Check for updates

A lead-free two-dimensional perovskite for a high-performance flexible photoconductor and a light-stimulated synaptic device†

Liu Qian,‡[a,b,c] Yilin Sun,‡[d] Mingmao Wu,[a] Chun Li, [ID][a] Dan Xie,*[d] Liming Ding [ID] *[b,c] and Gaoquan Shi [ID] *[a]

Organo-lead halide perovskites have emerged as promising materials for high-performance photodetectors. However, the toxicity of lead cations in these materials limits their further applications. Here, a flexible photoconductor is developed based on lead-free two-dimensional (2D) perovskite $(PEA)_2SnI_4$ *via* a one-step solution processing method. The flexible transparent electrodes are patterned from rGO/(PEDOT:PSS) hybrid films. The stability and reproducibility of the devices are significantly improved on adding 30 mol% SnF_2 to the perovskite. The flexible photoconductors show a photoresponsivity of 16 A W^{-1} and a detectivity of 1.92×10^{11} Jones under 470 nm illumination, which are higher than those of most of the similar devices. Besides, the devices possess much better mechanical flexibility and durability than the flexible devices with an Au electrode. Finally, this flexible photoconductor is applied as a light-stimulated synaptic device and can mimic the short-term plasticity of biological synapses. This is the first study to report that lead-free 2D perovskite can be used in flexible photoconductors and synaptic devices.

Introduction

Organic–inorganic hybrid perovskites have been widely used as active layer materials in the field of optoelectronics, such as in solar cells,[1–3] light emitting diodes[4–6] and photodetectors.[7–9] In the past few years, photodetectors based on perovskite materials have shown good performance because of their good light absorption and high charge carrier mobility.[10,11] The solution processability of a perovskite makes it applicable in the fabrication of low-cost and flexible photodetectors. However, most reported high-performance photodetectors consist of lead halide perovskites, typically $CH_3NH_3PbI_3$, and the toxicity issue of lead remains a big issue. There is a demand to develop lead-free perovskite materials to produce environmentally friendly devices.

Great effort has been made to replace Pb^{2+} with other metal cations, such as Sn^{2+},[12,13] Ge^{2+},[14] Bi^{3+} (ref. 15 and 16) and Sb^{3+}.[17,18] Owing to the similar radii of Pb and Sn ions (Pb 1.49 Å and Sn 1.35 Å), Sn-containing perovskites are widely used in solar cells. But so far only a limited number of studies have focused on Sn perovskite photodetectors because of the decreased performance caused by their intrinsic defects, Sn-cation vacancies.[19] Sn^{2+} can be easily oxidized into Sn^{4+}, leading to self-doping of the material, as well as the poor stability and reproducibility of the devices.[20,21] Recently, two-dimensional (2D) layered perovskites have become a potential candidate material for use in high-performance and stable optoelectronic devices.[22,23] This kind of perovskites can be regarded as the derivatives of conventional 3D perovskites formed by replacing small methylammonium (MA^+) with large ammonium cations, such as butylammonium (BA^+) and phenylethylammonium (PEA^+). They usually show excellent air stability since the long organic chains can block the moisture ingress.[24] Tan *et al.* first reported a photodetector based on individual 2D perovskite crystals of $(BA)_2PbBr_4$.[25] The lead-free 2D perovskite $(PEA)_2SnI_4$ was initially utilized in field-effect transistors (FETs) because of its high carrier mobility.[26] Solution-processed $(PEA)_2SnI_4$ films exhibited a field-effect mobility of 0.62 cm^2 V^{-1} s^{-1}. Chen *et al.* used this 2D perovskite $(PEA)_2SnI_4$ to fabricate a visible light sensitive phototransistor and the device exhibited an ultrahigh photoresponse.[27] However, the device couldn't return to its dark state when the light was off because of the high conductivity caused by the self-doping effect. This perovskite shows effective light absorption in the

[a]Department of Chemistry, Key Laboratory of Bioorganic Phosphorus Chemistry & Chemical Biology (MOE), Tsinghua University, Beijing 100084, China. E-mail: gshi@tsinghua.edu.cn

[b]Center for Excellence in Nanoscience, Key Laboratory of Nanosystem and Hierarchical Fabrication (CAS), National Center for Nanoscience and Technology, Beijing 100190, China. E-mail: ding@nanoctr.cn

[c]University of Chinese Academy of Sciences, Beijing 100049, China

[d]Tsinghua National Laboratory for Information Science and Technology (TNList), Institute of Microelectronics, Tsinghua University, Beijing 100084, China. E-mail: xiedan@tsinghua.edu.cn

†Electronic supplementary information (ESI) available. See DOI: 10.1039/c8nr00914g

‡These authors contributed equally to this work.

visible range, and we think that it could be used in the fabrication of high-performance lead-free photodetectors.

Here, we report for the first time the fabrication of a flexible photoconductor based on lead-free 2D perovskite $(PEA)_2SnI_4$ through a one-step approach. The flexible electrodes were prepared by patterning the spin-coated rGO (reduced graphene oxide)/(PEDOT:PSS) hybrid films on polyethylene terephthalate (PET) substrates. The conductance of rGO is significantly enhanced due to the introduction of PEDOT:PSS. Sn vacancies were effectively reduced by the addition of SnF_2. The devices exhibited a photoresponsivity of $\sim$16 A W^{-1}, which is higher than most of the similar perovskite photoconductors. They can maintain the initial performance after 1500 cycles of bending. This lead-free photoconductor can be applied in light-controlled memory devices, which can mimic the short-term plasticity of biological synapses due to the existence of Sn vacancies.

Results and discussion

Fig. 1a shows a schematic illustration of the fabrication of flexible and transparent interdigitated electrodes. The rGO/(PEDOT:PSS) film was prepared by spin-coating their mixed solution followed by hydroiodic acid (HI) treatment. The changes of the hybrid film rGO-P60 (with 60 vol% PEDOT:PSS) after HI treatment can be detected by X-ray photoelectron spectroscopy (XPS) (Fig. S1, ESI†). The S 2p peak with a binding

energy of 168.2 eV originates from PSS, whereas those at 164.1 and 165.0 eV from the S atoms of PEDOT.[28] The intensity ratios of the S 2p peaks related to PSS and PEDOT decreased from 1.98 to 1.21 after HI treatment, indicating the loss of PSS from the film. Partial removal of the PSS component can increase the film conductivity. In addition, the Raman spectrum of the rGO-P60 film shows the obvious incorporation of PEDOT:PSS (peak at 1433 cm^{-1}) and a significant reduction of graphene oxide (GO) (I_D/I_G = 2.15), which can enhance the conductivity of the hybrid film (Fig. S2, ESI†). The surface morphology of the rGO-P60 film was studied by atomic force microscopy (AFM). The pristine rGO film has a smooth surface with wrinkles (Fig. S3a, ESI†) while the rGO-P60 film shows an rGO film with PEDOT:PSS particles (Fig. 1b and Fig. S3b, ESI†). After rGO/(PEDOT:PSS) coating, the patterns of the interdigitated electrodes were then obtained by photolithography and oxygen plasma etching (for details, see the Experimental section). The optical microscopy images of the interdigitated electrodes with different volume percentages of PEDOT:PSS are shown in Fig. S4 (ESI†). The pure PEDOT:PSS film could not be patterned by ICP (Inductively Coupled Plasma) etching because of its bad adhesion to the substrate, which led to broken and detached fingers (Fig. S4b, ESI†). The rGO/(PEDOT:PSS) hybrid film exhibits good mechanical strength and good conductivity. On increasing the PEDOT:PSS content, the sheet resistance of the hybrid film decreased (Fig. 1c). However, when the PEDOT:PSS content was more than 60 vol%, the electrode fingers were broken by oxygen plasma
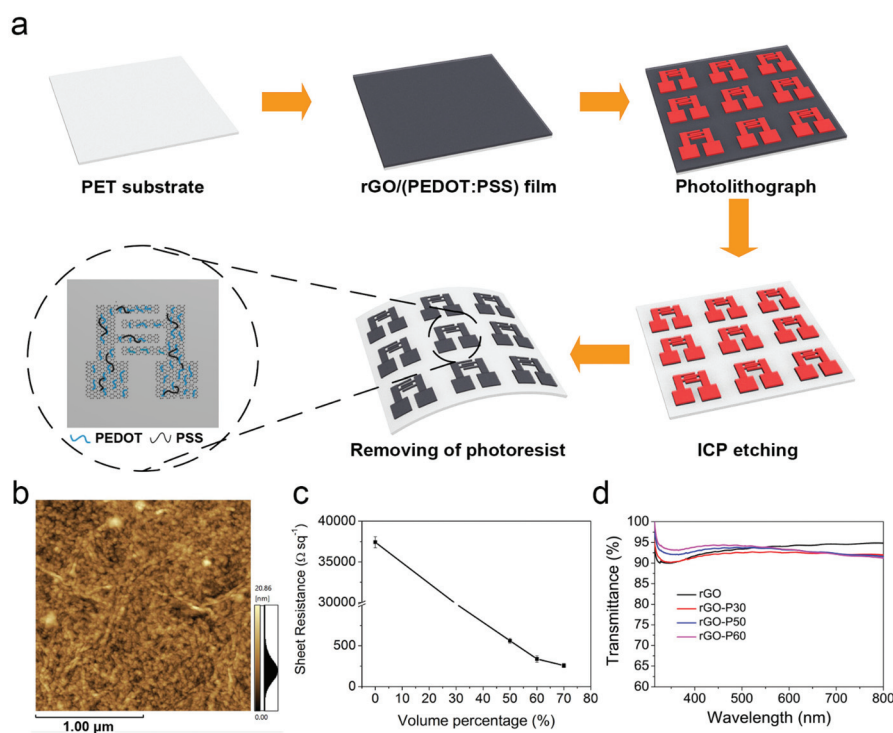

Fig. 1 (a) The fabrication process for rGO/(PEDOT:PSS) electrodes on the PET substrate; (b) AFM image for the rGO-P60 film; (c) sheet resistance for the films plotted against volume percentage of PEDOT:PSS in the solution; (d) transmittance spectra of rGO/(PEDOT:PSS) films.

(Fig. S4f†). So we used the rGO-P60 film to prepare flexible electrodes. An enlarged SEM image of the electrode fingers and the width are shown in Fig. S5 (ESI†). The transparency of the hybrid film was also studied. As shown in Fig. 1d, films with 0–60 vol% PEDOT:PSS exhibit good transmittance (>90% in the visible light range). The transmittance of the electrode substrate was around 80% in visible light (Fig. S6, ESI†).

The $(PEA)_2SnI_4$ solution was deposited onto the flexible electrodes *via* spin-coating. The crystal structure of $(PEA)_2SnI_4$ is illustrated in Fig. 2a. The inorganic layers comprise a single sheet of corner-sharing metal–halide octahedral, sandwiching layers of PEA^+ cations. Here we used the addition of SnF_2 to reduce the metallic conductivity of Sn perovskites. The X-ray diffraction (XRD) patterns of the perovskite film without or with 20–40 mol% SnF_2 display the same peaks at 5.4°, 10.8°, 16.2°, 21.8°, 27.4°, 33.0°, and 38.6°, which can be ascribed to the respective diffraction from the (0 0 *l*) (*l* = 2, 4, 6, 8, 10, 14) planes of the crystal (Fig. 2b). This indicated that the $(PEA)_2SnI_4$ crystal possesses a layered structure. The addition of SnF_2 did not result in a significant variation in the lattice parameters. F^- didn't substitute any I^- in the crystal due to the much smaller ionic radii of F^- than I^-.[29] The steady-state photoluminescence (PL) spectrum of the perovskite film without or with 20–40 mol% SnF_2 exhibited the same peak at 627 nm (Fig. 2c), suggesting that SnF_2 did not change the bandgap of the perovskite film. X-Ray photoelectron spectroscopy (XPS) was used to check the change of the perovskite component after adding SnF_2. As shown in Fig. 2d, the two peaks deconvoluted from the Sn 3d XPS spectra at 486.4 and 487.2 eV are associated with Sn^{2+} and Sn^{4+}, respectively.[30]

Films with 30 mol% SnF_2 exhibited a much lower amount of Sn^{4+} compared with the pristine perovskite film, implying a reduction of Sn vacancies with the addition of SnF_2. Actually, SnF_2 in Sn perovskites can increase the Sn chemical potential, which can increase the formation energy of Sn vacancies, reducing the concentration of these intrinsic defects.[29] The reduction of Sn vacancies was also confirmed by time-resolved photoluminescence (TRPL) decay curves (Fig. S7, ESI†). The PL decay in the pristine perovskite film was faster than that in the film with SnF_2, implying a strong recombination in the pristine film. The influence of SnF_2 addition on the film morphology was also investigated by scanning electron microscopy (SEM). Top view SEM images in Fig. 2e indicate a smooth surface of the pristine $(PEA)_2SnI_4$ film. 30 mol% addition of SnF_2 caused a change in grain shape. A higher content of SnF_2 led to more white particles on the film surface (Fig. S8d, ESI†). These particles might be new Sn–I–F compounds, according to the enlarged XRD patterns in Fig. S9 (ESI†).

The device architecture is illustrated in Fig. 3a. The photoresponse behaviour of the device was first studied under the illumination of 470 nm monochromatic light. A pristine $(PEA)_2SnI_4$ device had a high dark current because Sn vacancies caused metallic conduction (Fig. S10a, ESI†). Although the device responds to 470 nm illumination effectively, the photocurrent decays under continuous 5 V bias voltage. The vacancy migration might interrupt the conducting channel. After the addition of SnF_2, the amount of Sn vacancies was reduced and the device became less conductive but more stable (Fig. S10b–d, ESI†). The perovskite with 30 mol% SnF_2 was used to study the photoresponse perform-
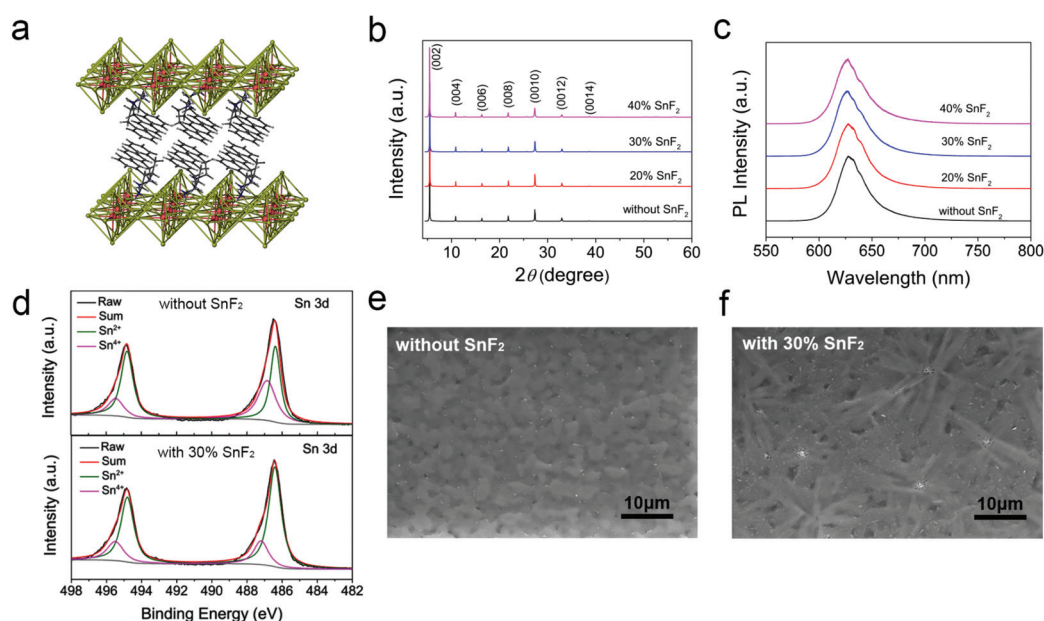
Fig. 2 (a) Crystal structure of 2D layered $(C_6H_5CH_2CH_2NH_3)_2SnI_4$ (orange balls, tin atoms; yellow balls, iodine atoms; blue balls, nitrogen atoms; dark grey balls, carbon atoms; light grey balls, hydrogen atoms); (b) XRD patterns of perovskite films with different SnF_2 contents; (c) photoluminescence spectra of perovskite films with different SnF_2 contents; (d) Sn 3d XPS spectra of perovskite layers without (top) or with (bottom) 30 mol% SnF_2. Top-view SEM image of the perovskite film without (e) or with (f) 30 mol% SnF_2.
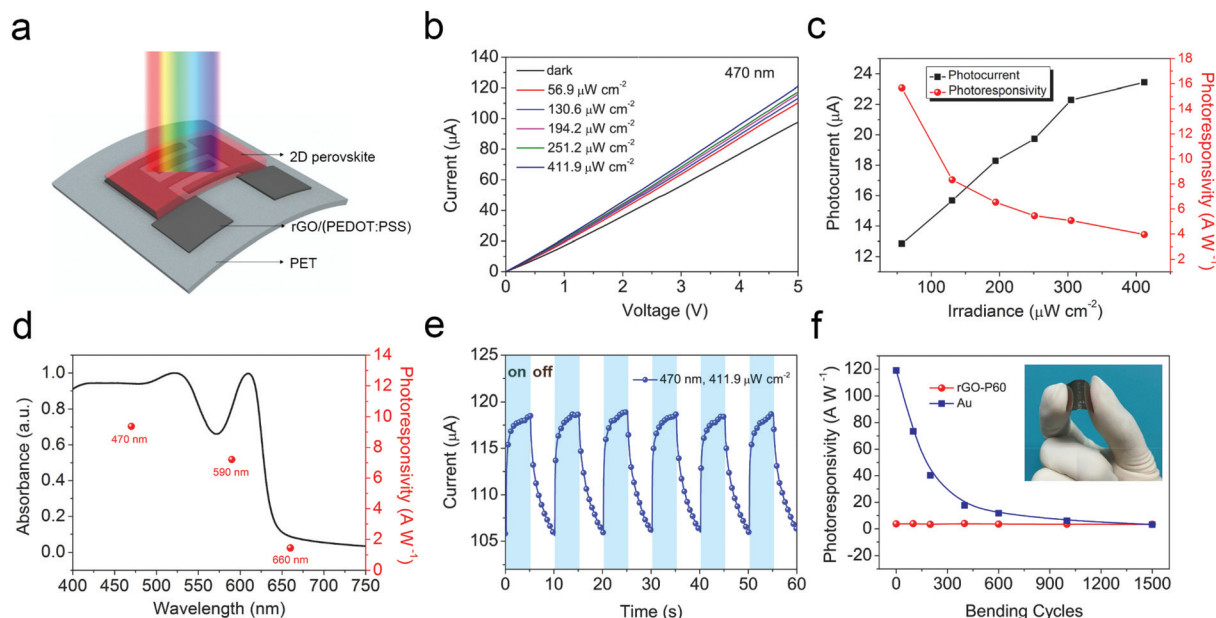
Fig. 3 Photoresponse of the (PEA)$_2$SnI$_4$ flexible photoconductor. (a) The structure of a (PEA)$_2$SnI$_4$ flexible photoconductor; (b) I–V curves in the dark or under different irradiances (470 nm); (c) plots of the photocurrent and photoresponsivity against irradiance at 5 V bias (470 nm light); (d) absorption spectrum of the perovskite film (with 30 mol% SnF$_2$) and the corresponding photoresponsivity at 470 nm, 590 nm and 660 nm (130 μW cm^{-2} irradiance, 5 V bias); (e) the time dependence of current for the flexible device at 5 V bias (412 μW cm^{-2} irradiance at 470 nm, with 5 s intervals); (f) plots of photoresponsivity against the bending cycle number for the flexible device with the Au electrode or the rGO-P60 electrode (5.5 mm radius, 412 μW cm^{-2} irradiance at 470 nm).

ance of the flexible devices. The concentration of the perovskite precursor solution was optimized to 0.3 mol L^{-1} (Fig. S12, ESI†). Fig. 3b shows the typical I–V curves of a device in the dark or under different irradiances at 470 nm. The plots indicate an ohmic contact between the (PEA)$_2$SnI$_4$ film and rGO/(PEDOT:PSS) electrodes. The highest occupied molecular orbital (HOMO) and the lowest unoccupied molecular orbital (LUMO) energy levels of the (PEA)$_2$SnI$_4$ film, and the work functions of the (PEA)$_2$SnI$_4$ film and electrodes were measured by ultraviolet photoelectron spectroscopy (UPS) (Fig. S13 and S14a, ESI†). The energy level diagram of the two materials is shown in Fig. S14b (ESI†). On decreasing the light irradiance, the photocurrent decreased, while the photoresponsivity increased (Fig. 3c). At a bias voltage of 5 V and a light irradiance of 56.9 μW cm^{-2}, this device delivered a photoresponsivity (R) of 16 A W^{-1}. The corresponding specific detectivity (D^*) was calculated to be 1.92×10^{11} Jones based on its noise current (I_n) (Fig. S15, ESI†). The performance of this

device is much better than that of most of the reported flexible perovskite photoconductors (Table 1). The photoconductive gain in the device resulted from the high charge carrier mobility of (PEA)$_2$SnI$_4$ and good ohmic contact between perovskite and the electrodes.

The photoresponse characteristics of the device were investigated at 470 nm, 550 nm and 660 nm with a fixed irradiance of 130 μW cm^{-2} at 5 V bias. As shown in Fig. 3d, the photoresponsivity of the device at different wavelengths correlates to the absorption spectrum of the (PEA)$_2$SnI$_4$ film. Fig. 3e shows the photoswitching performance of this perovskite photoconductor. The current was measured at 5 V bias under an irradiance of 412 μW cm^{-2} at 470 nm with 5 s intervals. When the light was on, a sudden increase of current was detected, which resulted from the photocurrent generated in the perovskite film. The rise time was determined to be ~0.63 s (Fig. S16, ESI†). The photocurrent was dominated by holes because a part of the electrons could be trapped in Sn vacancies.

Table 1 Comparison of the critical parameters of flexible perovskite photodetectors

| Structure	Wavelength [nm]	R [mA W^{-1}]	Rise time [ms]	Decay time [ms]	Ref.
PET/MAPbI$_3$ NW/silver paste	532	3×10^{-4}	120	210	31
PET/Au/MAPbI$_3$/PDPP3T	650	~100	40	140	32
PET/Au/MAPbI$_3$	650	100	0.3	0.4	33
C/TiO$_2$/MAPbI$_3$/Spiro/Au	550	101.5	<200	<200	34
ITO/MAPbI$_3$/ITO	365	3.49×10^3	<200	<200	35
	780	36.7	<100	<100	
(rGO/PEDOT:PSS)/(PEA)$_2$SnI$_4$	470	1.6×10^4	630	3600	This work

However, when the light was off, the photocurrent decreased slowly and showed a relatively long relaxation time (~3.6 s). This long decay time of the device was caused by the slow release of electrons trapped in the vacancies.[27]

The flexibility of this device was compared with a device on the Au/PET electrode. Without bending, the higher responsivity of Au devices (Fig. 3f) was due to the higher conductivity of Au, energy level matching of Au and perovskite (Fig. S14b†) and fewer defects at the Au/perovskite interface. However, when the device was bended repeatedly to a radius of 5.5 mm, the performance of the Au device decreased continuously, while the rGO/(PEDOT:PSS) device showed nearly no change with the bending cycles increasing. After 1500 bending cycles, the performance of the Au device decreased to the same level of the rGO/(PEDOT:PSS) device and it will decrease more on further bending cycles. The devices with rGO/(PEDOT:PSS) electrodes have much better mechanical flexibility and durability. The inset of Fig. 3f is a picture of the flexible device with the rGO/(PEDOT:PSS) electrode.

Though the inevitable Sn-cation vacancies lead to a relatively long decay time when illumination is off, this perovskite can be used in synaptic devices. The biological synapses can store and process information simultaneously *via* tuning the connection between two neighboring neurons. Inspired by this system, many artificial synaptic devices have been developed based on either transistors[36,37] or memristors.[38,39] However, conventional synaptic devices work separately from the data acquisition sensors. The gap between current neuromorphic computing and effective signal convertors drives us to explore new structures and multifunctional elements to improve the efficiency of neural computation. Light stimulus can offer ultrafast processing speeds, robustness and superior connectivity between discrete computing modules.[40] In biological synapses, information can be transmitted between neurons *via* sending neurotransmitters from the presynaptic neuron to the postsynaptic neuron (Fig. 4a). In our proof-of-concept light stimulated synapse device (Fig. 3a), the light pulse can be regarded as pre-synaptic stimuli and the current as the synaptic weight. Light pulses can be transmitted to the device by generating an excitatory postsynaptic current (EPSC). In neuroscience, the synaptic modification relies on the spike duration time or spike rate. The duration-time-dependent ΔEPSC of the device are shown in Fig. 4b. ΔEPSC increased from 0.8 μA to 7.0 μA when increasing the light pulse duration time from 1 ms to 200 ms. Then, a series of light pulses with the same duration time (10 ms) but different irradiances were applied on the device. ΔEPSC decreased from 3.7 μA to 1.7 μA with decreasing irradiance (Fig. 4c). These phenomena are quite similar to those in a biological excitatory synapse.[41]

The efficiency of the human brain depends on synaptic plasticity, which is the biological basis for the brain to learn, memorize, and forget.[36] Synaptic plasticity can be categorized into two types, short-term plasticity (STP) and long-term plasticity (LTP), based on the retention time.[42] The STP is a
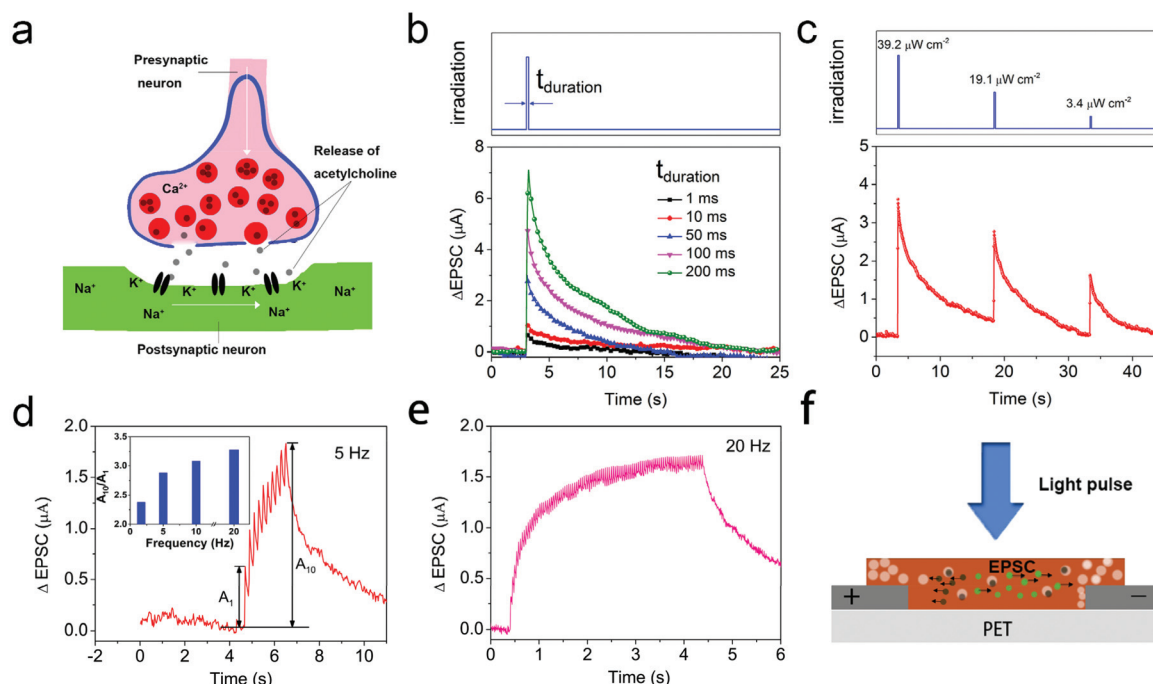
Fig. 4 (a) Schematic illustration of a biological synapse; (b) ΔEPSC under a 470 nm light pulse with different pulse durations (40 μW cm^{-2} irradiance); (c) ΔEPSC under several 470 nm light pulses with the same duration time (10 ms) and different irradiances (39.2, 19.1, and 3.4 μW cm^{-2}); (d) ΔEPSC under 10 light pulses with time intervals of 200 ms (including 10 ms duration time). The inset is a histogram of frequency-dependent EPSC gain (A_{10}/A_1); (e) ΔEPSC under 100 light pulses with time intervals of 50 ms (including 10 ms duration time); (f) the scheme for the work mechanism of the 2D perovskite based synaptic device (white balls for vacancies; black balls for electrons; green balls for holes).

temporal memory of the synaptic connection, which lasts for several minutes or less and finally returns to the initial state. The dynamic synaptic behaviors of our device were studied (Fig. 4d). When the device was simulated by 10 light pulses with time intervals of 200 ms (including a light duration time of 10 ms), the peak value of EPSC triggered by one pulse was larger than the previous one. And when the light was off, the EPSC decayed to the initial current. This can be regarded as a mimic of the STP of a biological excitatory synapse. The frequency dependent synaptic transmission was studied using 10 light pulses with different frequencies (2 Hz, 5 Hz, 10 Hz, and 20 Hz, Fig. S17, ESI†). The light pulse frequency dependence of EPSC gain (A_{10}/A_1) is shown in Fig. 4d. The gain increased with the increasing frequency. Fig. 4e shows the ΔEPSC changes with time (100 light pulses, 20 Hz frequency), and the current can get saturated. Fig. S18† also indicates the good working stability of the device.

The working mechanism of this synaptic device relates to the Sn vacancies in $(PEA)_2SnI_4$ perovskite material. When the first light pulse was on, the free charge carriers were generated, and some electrons could be trapped by those vacancies. The trapped electrons could lead to an augment of the number of holes generated by the second pulse.[41] According to this mechanism, the device performance is quite similar to the STP behavior of the biological synapse.

Conclusions

In summary, a flexible photoconductor based on lead-free 2D perovskite $(PEA)_2SnI_4$ was developed *via* a solution processing approach. The transparent flexible electrodes were made by patterning the rGO/(PEDOT:PSS) hybrid film on PET substrates. In order to reduce Sn vacancies in the material, 30 mol% SnF_2 was added, and the devices presented high stability and reproducibility. The device demonstrated a photoresponsivity of 16 A W^{-1} and a detectivity of 1.92×10^{11} Jones under 470 nm light illumination. This photoconductor may be used as a light stimulated synaptic device. Further work will focus on the study of the LTP and inhibitory behavior of 2D perovskite based devices.

Conflicts of interest

There are no conflicts to declare.

Acknowledgements

Notes and references

1 J. Burschka, N. Pellet, S. J. Moon, R. Humphry-Baker, P. Gao, M. K. Nazeeruddin and M. Gratzel, *Nature*, 2013, **499**, 316–319.
2 H. Zhou, Q. Chen, G. Li, S. Luo, T.-B. Song, H.-S. Duan, Z. Hong, J. You, Y. Liu and Y. Yang, *Science*, 2014, **345**, 542–546.
3 Q. Jiang, Z. Chu, P. Wang, X. Yang, H. Liu, Y. Wang, Z. Yin, J. Wu, X. Zhang and J. You, *Adv. Mater.*, 2017, **29**, 1703852.
4 Y. H. Kim, H. Cho, J. H. Heo, T. S. Kim, N. Myoung, C. L. Lee, S. H. Im and T. W. Lee, *Adv. Mater.*, 2015, **27**, 1248–1254.
5 J. Wang, N. Wang, Y. Jin, J. Si, Z. K. Tan, H. Du, L. Cheng, X. Dai, S. Bai and H. He, *Adv. Mater.*, 2015, **27**, 2311–2316.
6 L. Zhang, X. Yang, Q. Jiang, P. Wang, Z. Yin, X. Zhang, H. Tan, Y. M. Yang, M. Wei, B. R. Sutherland, E. H. Sargent and J. You, *Nat. Commun.*, 2017, **8**, 15640.
7 L. Qian, Y. Sun, M. Wu, D. Xie, L. Ding and G. Shi, *Adv. Mater.*, 2017, **29**, 1606175.
8 W. Hu, W. Huang, S. Yang, X. Wang, Z. Jiang, X. Zhu, H. Zhou, H. Liu, Q. Zhang, X. Zhuang, J. Yang, D. H. Kim and A. Pan, *Adv. Mater.*, 2017, **29**, 1703256.
9 Y. Lee, J. Kwon, E. Hwang, C. H. Ra, W. J. Yoo, J. H. Ahn, J. H. Park and J. H. Cho, *Adv. Mater.*, 2015, **27**, 41–46.
10 C. Zuo, H. J. Bolink, H. Han, J. Huang, D. Cahen and L. Ding, *Adv. Sci.*, 2016, **3**, 1500324.
11 C. Wehrenfennig, G. E. Eperon, M. B. Johnston, H. J. Snaith and L. M. Herz, *Adv. Mater.*, 2014, **26**, 1584–1589.
12 Y. Ogomi, A. Morita, S. Tsukamoto, T. Saitho, N. Fujikawa, Q. Shen, T. Toyoda, K. Yoshino, S. S. Pandey, T. Ma and S. Hayase, *J. Phys. Chem. Lett.*, 2014, **5**, 1004–1011.
13 F. Hao, C. C. Stoumpos, R. P. Chang and M. G. Kanatzidis, *J. Am. Chem. Soc.*, 2014, **136**, 8094–8099.
14 T. Krishnamoorthy, H. Ding, C. Yan, W. L. Leong, T. Baikie, Z. Zhang, M. Sherburne, S. Li, M. Asta and N. Mathews, *J. Mater. Chem. A*, 2015, **3**, 23829–23832.
15 B. W. Park, B. Philippe, X. Zhang, H. Rensmo, G. Boschloo and E. M. Johansson, *Adv. Mater.*, 2015, **27**, 6806–6813.
16 K. Eckhardt, V. Bon, J. Getzschmann, J. Grothe, F. M. Wisser and S. Kaskel, *Chem. Commun.*, 2016, **52**, 3058–3060.
17 B. Saparov, F. Hong, J.-P. Sun, H.-S. Duan, W. Meng, S. Cameron, I. G. Hill, Y. Yan and D. B. Mitzi, *Chem. Mater.*, 2015, **27**, 5622–5632.
18 C. Zuo and L. Ding, *Angew. Chem., Int. Ed.*, 2017, **56**, 6528–6532.
19 A. Waleed, M. M. Tavakoli, L. Gu, Z. Wang, D. Zhang, A. Manikandan, Q. Zhang, R. Zhang, Y. L. Chueh and Z. Fan, *Nano Lett.*, 2017, **17**, 523–530.
20 F. Zuo, S. T. Williams, P. W. Liang, C. C. Chueh, C. Y. Liao and A. K. Jen, *Adv. Mater.*, 2014, **26**, 6454–6460.

21 T. Yokoyama, D. H. Cao, C. C. Stoumpos, T. B. Song, Y. Sato, S. Aramaki and M. G. Kanatzidis, *J. Phys. Chem. Lett.*, 2016, **7**, 776–782.

22 D. H. Cao, C. C. Stoumpos, O. K. Farha, J. T. Hupp and M. G. Kanatzidis, *J. Am. Chem. Soc.*, 2015, **137**, 7843–7850.

23 I. C. Smith, E. T. Hoke, D. Solis-Ibarra, M. D. McGehee and H. I. Karunadasa, *Angew. Chem., Int. Ed.*, 2014, **53**, 11232–11235.

24 S. Chen and G. Shi, *Adv. Mater.*, 2017, **29**, 1605448.

25 Z. Tan, Y. Wu, H. Hong, J. Yin, J. Zhang, L. Lin, M. Wang, X. Sun, L. Sun, Y. Huang, K. Liu, Z. Liu and H. Peng, *J. Am. Chem. Soc.*, 2016, **138**, 16612–16615.

26 C. Kagan, D. Mitzi and C. Dimitrakopoulos, *Science*, 1999, **286**, 945–947.

27 C. Chen, X. Zhang, G. Wu, H. Li and H. Chen, *Adv. Opt. Mater.*, 2017, **5**, 1600539.

28 Y. Xia, K. Sun and J. Ouyang, *Adv. Mater.*, 2012, **24**, 2436–2440.

29 M. H. Kumar, S. Dharani, W. L. Leong, P. P. Boix, R. R. Prabhakar, T. Baikie, C. Shi, H. Ding, R. Ramesh, M. Asta, M. Graetzel, S. G. Mhaisalkar and N. Mathews, *Adv. Mater.*, 2014, **26**, 7122–7127.

30 T. B. Song, T. Yokoyama, C. C. Stoumpos, J. Logsdon, D. H. Cao, M. R. Wasielewski, S. Aramaki and M. G. Kanatzidis, *J. Am. Chem. Soc.*, 2017, **139**, 836–842.

31 P. Zhu, S. Gu, X. Shen, N. Xu, Y. Tan, S. Zhuang, Y. Deng, Z. Lu, Z. Wang and J. Zhu, *Nano Lett.*, 2016, **16**, 871–876.

32 S. Chen, C. Teng, M. Zhang, Y. Li, D. Xie and G. Shi, *Adv. Mater.*, 2016, **28**, 5969–5974.

33 H. Deng, X. Yang, D. Dong, B. Li, D. Yang, S. Yuan, K. Qiao, Y.-B. Cheng, J. Tang and H. Song, *Nano Lett.*, 2015, **15**, 7963–7969.

34 H. Sun, T. Lei, W. Tian, F. Cao, J. Xiong and L. Li, *Small*, 2017, **13**, 1701042.

35 X. Hu, X. Zhang, L. Liang, J. Bao, S. Li, W. Yang and Y. Xie, *Adv. Funct. Mater.*, 2014, **24**, 7373–7380.

36 C. S. Yang, D. S. Shang, N. Liu, G. Shi, X. Shen, R. C. Yu, Y. Q. Li and Y. Sun, *Adv. Mater.*, 2017, **29**, 1700906.

37 P. Gkoupidenis, N. Schaefer, B. Garlan and G. G. Malliaras, *Adv. Mater.*, 2015, **27**, 7176–7180.

38 D. B. Strukov, G. S. Snider, D. R. Stewart and R. S. Williams, *Nature*, 2008, **453**, 80–83.

39 A. A. Bessonov, M. N. Kirikova, D. I. Petukhov, M. Allen, T. Ryhanen and M. J. Bailey, *Nat. Mater.*, 2015, **14**, 199–204.

40 D. Rosenbluth, K. Kravtsov, M. P. Fok and P. R. Prucnal, *Opt. Express*, 2009, **17**, 22767–22772.

41 S. Qin, F. Wang, Y. Liu, Q. Wan, X. Wang, Y. Xu, Y. Shi, X. Wang and R. Zhang, *2D Mater.*, 2017, **4**, 035022.

42 H. K. Li, T. P. Chen, P. Liu, S. G. Hu, Y. Liu, Q. Zhang and P. S. Lee, *J. Appl. Phys.*, 2016, **119**, 244505.